

See discussions, stats, and author profiles for this publication at: <https://www.researchgate.net/publication/243374922>

# Influence of Co <sup>2+</sup> Ion Concentration on the Size, Magnetic Properties, and Purity of CoFe <sub>2</sub> O <sub>4</sub> Spinel Ferrite Nanoparticles

ARTICLE *in* THE JOURNAL OF PHYSICAL CHEMISTRY C · APRIL 2010

Impact Factor: 4.77 · DOI: 10.1021/jp911966p

---

CITATIONS

62

---

READS

187

## 6 AUTHORS, INCLUDING:



**Ayyappan Sathya**

Istituto Italiano di Tecnologia

15 PUBLICATIONS 360 CITATIONS

SEE PROFILE



**Chandramohan Palogi**

Bhabha Atomic Research Centre

31 PUBLICATIONS 307 CITATIONS

SEE PROFILE



**John Philip**

Indira Gandhi Centre for Atomic Research

179 PUBLICATIONS 3,142 CITATIONS

SEE PROFILE

# Influence of $\text{Co}^{2+}$ Ion Concentration on the Size, Magnetic Properties, and Purity of $\text{CoFe}_2\text{O}_4$ Spinel Ferrite Nanoparticles

S. Ayyappan,<sup>†</sup> S. Mahadevan,<sup>†</sup> P. Chandramohan,<sup>‡</sup> M. P. Srinivasan,<sup>‡</sup> John Philip,<sup>\*,†</sup> and Baldev Raj

SMARTS, Metallurgy and Materials Group, Indira Gandhi Centre for Atomic Research, Kalpakkam 603 102, TN, India, Water and Steam Chemistry Division, BARC Facility, Kalpakkam 603 102, TN, India

Received: December 18, 2009; Revised Manuscript Received: March 4, 2010

Cobalt ferrite nanoparticles of different sizes are prepared by varying the concentration of  $\text{Co}^{2+}$  metal ions using precipitation approach. The average crystallite size, coercivity ( $H_C$ ), and saturation magnetization ( $M_S$ ) increases from 11 to 16 nm, 0.12 to 0.8 kOe, and 28 to 52 emu/g, respectively, as  $\text{Co}^{2+}$  ion concentration is reduced from 0.4 to 0.025 M. High resolution transmission electron microscopy and X-ray diffraction analysis confirms that  $\text{CoFe}_2\text{O}_4$  nanoparticles are crystalline in nature with cubic structure. Raman spectroscopic investigation shows traces of paramagnetic ferrihydrite in samples prepared with  $\text{Co}^{2+}$  ion concentration greater than 0.1 M. These experimental results suggest that metal ion concentration plays an important role in the size, magnetic property and purity of precipitated cobalt ferrite nanoparticles. The variation in the average crystalline size with  $\text{Co}^{2+}$  ion concentration is in good agreement with the nucleation theory. Our approach is useful in tuning the size and magnetic properties of cobalt ferrite nanoparticles.

## I. Introduction

Miniaturization of devices due to advancements in nanotechnology led to an increased interest in size dependent physical properties of nanomaterials.<sup>1,2</sup> Transition metal oxides with spinel structure  $\text{MFe}_2\text{O}_4$  ( $M = \text{Mn, Fe, Co, Ni, Zn, etc.}$ ) have attracted considerable interest during the last few decades due to their potential applications in high density storage devices, ferrofluids, microwave absorption, humidity sensor, photo detectors, etc.<sup>3–8</sup> Further magnetically polarizable nanofluids have been used as a model systems for fundamental studies and practical applications.<sup>9,10</sup> Exploiting the unique magnetic properties of  $\text{CoFe}_2\text{O}_4$  nanoparticles (e.g., tunable coercivity, large anisotropy, moderate saturation magnetization, unique light-induced coercivity change, site specific and strong binding to the serum albumin proteins etc.) many interesting biomedical applications are developed e.g. drug delivery, DNA separation, magnetic Resonance Image (MRI) contrast and hyperthermia.<sup>11–16</sup> Further, due to the strong spin–orbital angular momentum (L–S) coupling,  $\text{CoFe}_2\text{O}_4$  nanoparticles are highly stable up to 1000 °C and have good wear resistance and electrical insulation property.<sup>17,18</sup>

Easy methods to tailor nanoparticles of desired size, composition, purity, and physical properties are extremely important for practical applications. For ferrite nanoparticles, methods of controlling crystal size within the superparamagnetic and single domain limits are important. Several synthesis methods are developed to produce  $\text{CoFe}_2\text{O}_4$  nanoparticles that include hydrothermal,<sup>19</sup> solvothermal,<sup>20,21</sup> mechanical milling,<sup>22,23</sup> micellar method,<sup>24,25</sup> sol–gel,<sup>26</sup> Langmuir–Blodgett,<sup>27</sup> bacterial synthesis,<sup>28</sup> and coprecipitation method.<sup>29,30</sup> New synthesis routes are also developed to obtain  $\text{CoFe}_2\text{O}_4$  nanoparticles with

different morphologies such as nanocube, nanowire, thin films, nanoribbons, nanorods, etc.<sup>31,32</sup> Among these synthesis methods, chemical coprecipitation is one of the versatile techniques. Coprecipitation reaction consists of nucleation followed by particle growth and are strongly affected by precipitation conditions.<sup>33</sup> These two inseparable and instantaneous processes govern the shape of the final product. An understanding of the effects of various aspects such as stirring speed, temperature, nature of alkali, addition rate, digestion time, pH of the reactants etc. in coprecipitation is important to obtain nanoparticles of desired size and morphology.<sup>30,34–36</sup> Several theoretical and experimental studies have been aimed at understanding the aging phenomena and reaction rate during precipitation reactions.<sup>16,37</sup> Use of computer simulation for calculating the rates of both homogeneous and heterogeneous nucleation on microscopic impurities has been elegantly demonstrated recently.<sup>38</sup> Particles of larger than 40 nm (single domain size of  $\text{CoFe}_2\text{O}_4$  nanoparticles) divide into domains and domain wall moments results in a decrease in coercivity. Recent studies are focused on novel synthesis techniques to tune  $H_C$ <sup>3,18,22,36,39–42</sup> with superparamagnetic single domain<sup>43</sup> and polycrystalline multi domain particles.<sup>44</sup> Often low saturation magnetization and change in coercivity of ferrites are wrongly interpreted as arising from the dead layer contributions, though it can originates from traces of nonmagnetic impurities such as ferrihydrites, antiferromagnetic  $\alpha\text{-Fe}_2\text{O}_3$  etc. Though the  $\alpha\text{-Fe}_2\text{O}_3$  can be distinguished from XRD, it is difficult to be distinguished from standard XRD peaks of  $\text{CoFe}_2\text{O}_4$  phase. Lin et al,<sup>35</sup> reported that the size induced magnetic properties of surface modified  $\text{CoFe}_2\text{O}_4$  nanoparticles can be obtained by varying the ammonia concentration and temperature. However, an excess amount of  $\text{Fe}^{3+}$  at higher concentration of alkali and higher temperature can lead to the formation of paramagnetic ferrihydrite phase that can lead to less saturation magnetization and coercivity values.<sup>45</sup> Pramanik et al.<sup>26</sup> studied the effect of  $[\text{Co}^{2+}]$  to  $[\text{Fe}^{3+}]$  ratio on the formation of  $\text{Co}_{1+x}\text{Fe}_{2-x}\text{O}_4$  thin films and found that an

\* Corresponding author. Fax: 91-44-27480356. E-mail: philip@igcar.gov.in.

<sup>†</sup> SMARTS.

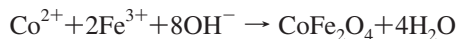
<sup>‡</sup> BARC Facility.

increasing [Co<sup>2+</sup>]/[Fe<sup>3+</sup>] molar ratio can lead to a decrease in the H<sub>C</sub> and the M<sub>S</sub>. Further, it has been found that the Curie temperature of the Co<sub>1+x</sub>Fe<sub>2-x</sub>O<sub>4</sub> films gradually increases with decreasing [Co<sup>2+</sup>]/[Fe<sup>3+</sup>] ratio, which is attributed to the magnetic coupling between Co<sub>1+x</sub>Fe<sub>2-x</sub>O<sub>4</sub> and α-Fe<sub>2</sub>O<sub>3</sub> phases. The lack of consensus on the size dependent H<sub>C</sub> and other magnetic properties of cobalt ferrites essentially originate from the polydispersity, composition and impurities present in the samples. In our previous study we demonstrated that the reduction in magnetic properties with size of CoFe<sub>2</sub>O<sub>4</sub> nanoparticles is mainly due to the formation of paramagnetic ferrihydrite phase with increasing digestion time. In this paper, we investigate the effect of Co<sup>2+</sup> metal ion concentration on size and magnetic properties of CoFe<sub>2</sub>O<sub>4</sub> nanoparticles. Metal ion concentration is varied from 0.4 to 0.025 M by taking 1:2 molar ratios of Co<sup>2+</sup> and Fe<sup>3+</sup> solutions.

## II. Experimental Section

The chemicals used are FeCl<sub>3</sub>·6H<sub>2</sub>O, CoCl<sub>2</sub>·6H<sub>2</sub>O, NaOH, oleic acid, 35% hydrochloric acid, hexane, and acetone. All chemicals used are GR grade (E-Merck) except hexane. Chemicals are used without any further purification. Water used is Elga water filtered with 0.22 μm size filter. The resistivity of the water is 18 MΩ-cm.

**A. Synthesis of CoFe<sub>2</sub>O<sub>4</sub> Nanoparticles.** Synthesis of CoFe<sub>2</sub>O<sub>4</sub> nanoparticles is carried out by precipitating freshly prepared (GR grade) 0.4 M Co<sup>2+</sup> and 0.8 M Fe<sup>3+</sup> salt solutions of stoichiometric proportions in alkaline medium at constant stirring. The solution pH is rapidly increased to 12, by the addition of 6N NaOH at 90 °C. The chemical reaction can be written as



The addition of alkali is carried out at a constant rate of 20 mL/s. After 1 h. of digestion, oleic acid is added to coat the precipitated particles at lower a pH of 9 and the mixture is left for 30 min at relatively lower temperature of 70 °C. Then, the pH of the dispersion is adjusted to ~6–7, with dilute HCl. As protonation occurs, the particles are separated from the dispersion. The obtained particles are washed with water at 60 °C on vigorous stirring for several times, until they are free from ionic impurities. After protonation is complete, the black precipitate is separated from the solution and decanted with water to eliminate the excess salts from the solution. Further purification is done by washing the particles with hexane and acetone mixture and then centrifuged at 2500 rpm for 30 min. This procedure is repeated for three times. Finally, CoFe<sub>2</sub>O<sub>4</sub> nanoparticles are dried at 35 °C for 24 h in an inert atmosphere. The dried particles are used for further characterization. Different sizes of CoFe<sub>2</sub>O<sub>4</sub> nanoparticles are prepared by using the same synthesis protocol except by taking different concentration of Co<sup>2+</sup> (0.4 to 0.025 M) and Fe<sup>3+</sup> (0.8 to 0.05 M) salt solution. The activity of ion is the product of activity coefficient and concentration of the metal ion. At the concentration range of 0.4–0.025 M, Co<sup>2+</sup> metal ion activity ranges from 28 to 0.19 mM.

**B. Characterization.** A MAC Science MXP18 X-ray diffractometer was used for crystal structure and average particle size analysis. 2θ values were taken from 15 to 65° using CuK<sub>α</sub> radiation (λ value of 1.5406 Å). The XRD patterns of nanoparticles were verified by comparing with the JCPDS card no. 22-1086. High resolution transmission electron microscopy

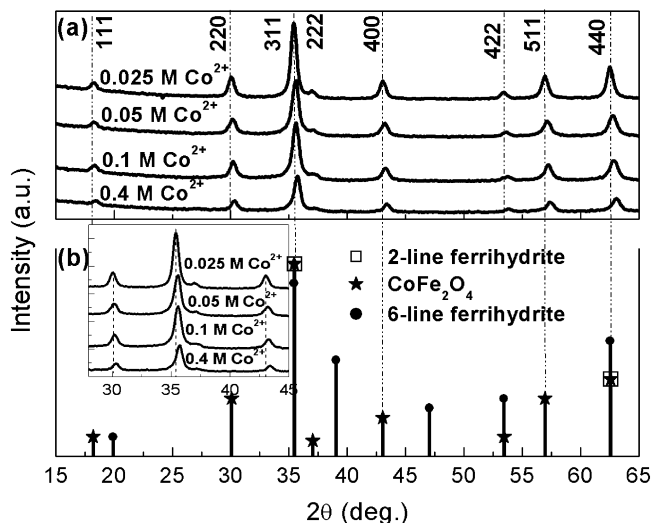


**Figure 1.** (a) Powder X-ray diffraction pattern of CoFe<sub>2</sub>O<sub>4</sub> nanoparticles prepared at different Co<sup>2+</sup> ion concentrations of 0.4, 0.1, 0.05, and 0.025 M. (b) Standard peaks of CoFe<sub>2</sub>O<sub>4</sub> nanoparticles (solid star), 2-line ferrihydrite (open square), and 6-line ferrihydrite (solid circle). Vertical dotted lines are a guide to the eye. The inset of panel b shows the magnified view of the peaks in the 2θ range of 30–45°.

(HRTEM) investigations were carried out using a JEOL 2000 EX II (T) operated at 200 kV. One drop of colloidal suspension of CoFe<sub>2</sub>O<sub>4</sub> in hexane is deposited in to a carbon film coated copper grid, and dried overnight under a lamp. The particle size and distribution is measured by Dynamic Light Scattering (DLS) using Malvern Nano ZS at 25 °C. Atomic Absorption Spectroscopy (AAS) for the samples are carried out using a double beam atomic absorption spectrometer (AAS), GBC model Avanta. BOMEM MB 100 FTIR spectrometer, operated in the spectral range 4000–400 cm<sup>-1</sup> at a resolution of 1 cm<sup>-1</sup> to identify the binding of oleic acid on CoFe<sub>2</sub>O<sub>4</sub> nanoparticle surface. A TGA/DSC1 (Mettler Toledo Ltd.) instrument is used for weight loss measurements in air atmosphere. A heating rate of 10 °C min<sup>-1</sup> is maintained throughout the measurements. Vibrating sample magnetometer (Lake Shore Ltd. Model: 7404) is used for magnetization measurements in the applied magnetic field range of –15 to 15 kG. Micro Raman spectra were recorded with a HR800 (Jobin Yvon Ltd.) micro spectrometer. A small quantity of the sample is placed in a glass slide on the microscopy stage. A 514 nm Ar ion laser was used for excitation of the sample. The power incident on the sample surface was about 0.5 mW, with a laser spot size of about 1.5 μm with 100× objective. Dispersion of the Raman scattering was achieved through an 1800 gr mm<sup>-1</sup> grating. Data acquisition was done in the range of 100–2000 cm<sup>-1</sup> from the laser line for 10 s.

## III. Results and Discussion

**A. Structural Analysis and Size Distribution of CoFe<sub>2</sub>O<sub>4</sub> Nanoparticles by XRD, TEM, and DLS.** Figure 1 shows the XRD pattern of CoFe<sub>2</sub>O<sub>4</sub> nanoparticles synthesized at different Co<sup>2+</sup> metal ion concentration. The sharp peaks from diffraction patterns show the crystalline nature of the samples. The diffraction peaks from (111), (220), (311), (222), (400), (422), (511), and (440) crystal plane confirm the cubic spinel structure and the major peaks match with the standard pattern of bulk CoFe<sub>2</sub>O<sub>4</sub> (JCPDS 22-1086). Atomic absorption spectra confirm that the amount of Co and Fe contents in CoFe<sub>2</sub>O<sub>4</sub> nanoparticles is 216 and 398 μg/mL, respectively. This confirms the correct stoichiometry of CoFe<sub>2</sub>O<sub>4</sub> nanoparticles with 1:2 ratio of Co

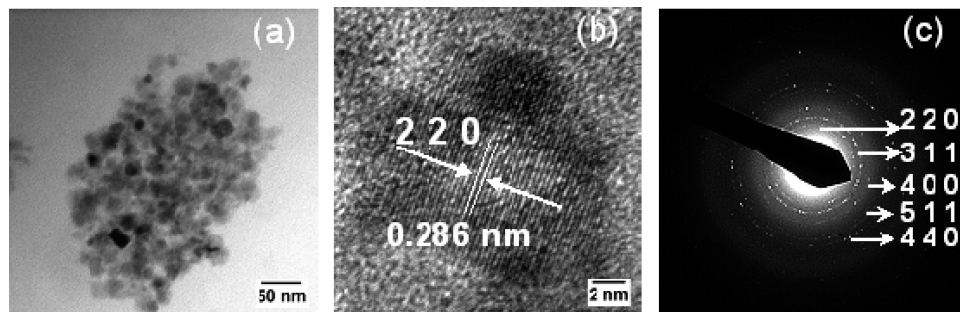


**Figure 2.** (a) TEM image of  $\text{CoFe}_2\text{O}_4$  nanoparticles synthesized at a  $\text{Co}^{2+}$  concentration of 0.025 M. (b) HRTEM lattice image from a single  $\text{CoFe}_2\text{O}_4$  nanoparticles. (c) Selected area electron diffraction (SAED) of the specimen showing diffuse rings from  $\text{CoFe}_2\text{O}_4$  reflections.

and Fe. For comparison, the characteristic peaks of 2-line ferrihydrite and 6-line ferrihydrite are also shown in the lower part of the XRD pattern (Figure 1). It can be seen that a few peaks of  $\text{CoFe}_2\text{O}_4$ —(311), (422), and (440)—and 6-line ferrihydrite overlaps. Many of the conflicting reports on magnetic properties of  $\text{CoFe}_2\text{O}_4$  originate from the fact that detailed analysis on the impurities present in  $\text{CoFe}_2\text{O}_4$  (such as 2-line ferrihydrite and 6-line ferrihydrite) was not carried out. The average crystalline size increases from 11 to 16 nm as the  $\text{Co}^{2+}$  concentration is decreased from 0.4 to 0.025 M. The lattice parameter (a) for 0.4, 0.1, 0.05, and 0.025 M  $\text{Co}^{2+}$  ion concentrations are 8.364, 8.365, 8.369, and 8.389 Å, respectively. Estimated values of lattice constants from the XRD pattern are in good agreement with the reported value of 8.391 Å. Shifting in peak position toward lower  $2\theta$  is due to the increase in the lattice parameter. Such behavior has been observed in  $\text{CoFe}_2\text{O}_4$  nanoparticles synthesized by varying the addition rate of NaOH, where the crystal size is varied from 31 to 24 nm.<sup>36</sup> A similar effect is also observed by Gu et al.<sup>46</sup> in  $\text{CoFe}_2\text{O}_4$  nanoparticles in the size range of 9–30 nm, synthesized by varying the metal ion concentration from 0.1 to 0.5 M. They have attributed the peak shift to the cation distribution and magnetic properties. Similar results are obtained by other groups in  $\text{CoFe}_2\text{O}_4$ ,  $\text{ZnFe}_2\text{O}_4$ , and  $\text{NiFe}_2\text{O}_4$  systems.<sup>39,47,48</sup> In  $\text{NiFe}_2\text{O}_4$  the lattice constant decreases from 8.28 to 8.16 Å as the grain size is reduced from 40 to 3.5 nm.<sup>47</sup> Their positron lifetime measurements show that grain size affects the tetrahedral and octahedral site radii due to an abnormal lattice contraction. In  $\text{ZnFe}_2\text{O}_4$ , the lattice parameter is found to decrease monotonically with decreasing grain size; that is, the lattice parameter decreases from 8.448 to 8.267 Å as the grain size is reduced from bulk to 5 nm.<sup>48</sup> Among the available interstitial sites of  $\text{CoFe}_2\text{O}_4$ , eight of the A-sites occupied by  $\text{Fe}^{3+}$  ions and 16 of B-sites are occupied by 8  $\text{Co}^{2+}$  and 8  $\text{Fe}^{3+}$  ions and the remaining unoccupied may contain lattice vacancies. These vacancies in the crystal lattice may also contribute to the lattice contrast at lower size due to high surface tension.<sup>49,50</sup>

Figure 2a shows the transmission electron microscopy (TEM) image of  $\text{CoFe}_2\text{O}_4$  nanoparticles synthesized with 0.025 M  $\text{Co}^{2+}$ . The average diameter obtained from image analysis is 14.8 nm, against 16 nm obtained by XRD. The size obtained from XRD is generally larger than the size obtained from TEM because (1) the X-ray intensity is proportional to the average particle volume, while the particle size obtained from TEM images represents the average radius and (2) the size distributions obtained from TEM images are restricted to primary particles and do not include secondary particles formed by epitaxial attachment. Secondary particles are formed from integer multiples of primary particles and can have a significant influence on the volume distribution, even at relatively low concentration. Figure 2b,c shows HRTEM and the selected area electron

diffraction (SAED) pattern, respectively. The clear lattice boundary in HRTEM image illustrates the high crystallinity of  $\text{CoFe}_2\text{O}_4$  nanoparticles (Figure 2b). The periodic fringe spacing of 0.286 nm corresponds to the (220) plane of cubic  $\text{CoFe}_2\text{O}_4$ . This is well matched with the standard (JCPDS card no. 22-1086) value of 0.296 nm. The SAED pattern shows diffuse rings with less intensity that can be indexed to  $\text{CoFe}_2\text{O}_4$  [(220), (311), (400), (422), (511), and (440)] planes reflections.

During coprecipitation, simultaneous occurrence of nucleation, growth, coarsening, and agglomeration take place. Both the nucleation and growth govern the particle size and morphology of the precipitated products. The nucleated small crystallites tend to aggregate together to form more thermodynamically stable particles. Since it is difficult to isolate each processes occurring during precipitation, the fundamental understanding of coprecipitation are still in an infancy. The equilibrium critical radius,  $r^*$ , during a precipitation reactions is given by Gibbs–Thompson equation<sup>33</sup>

$$r^* = \frac{\alpha}{\Delta C} \quad (1)$$

Where  $\alpha$  is given by

$$\alpha = \frac{2\nu\sigma}{k_B T \ln(S)} \quad (2)$$

where  $S = (a_1 a_2)/K_{sp}$ ,  $\sigma$  is the interfacial surface energy,  $\nu$  is the molecular volume of the precipitated particles,  $k_B$  is Boltzmann constant,  $T$  is temperature,  $K_{sp}$  is solubility product constant,  $a_1$  and  $a_2$  are the activities of solute molecules, and  $S$  is the supersaturation. In other words,  $S = C/C_{eq}$  where,  $C$  and  $C_{eq}$  are the solute concentrations at saturation and equilibrium respectively. The difference in  $C$  and  $C_{eq}$  ( $\Delta C = C - C_{eq}$ ) is considered as the driving force for precipitation. If the nucleated particles have a radius with  $r > r^*$ , it will continue to grow while those with  $r < r^*$  will dissolve in the existing solution and grow further as per the Oswald ripening process. The Lifshitz–Slyozov–Wagner (LSW) theory provides a quantitative treatment of the time dependence of the particle growth.<sup>51,52</sup> For spherical particles, the solubility  $c_r$  of a particle of radius  $r$  is

$$c_r = c_\infty \exp\left(\frac{2\gamma V_m}{RT r}\right) \quad (3)$$

where  $c_\infty$  is the solubility at a flat surface,  $\gamma$  is the surface energy of the solid,  $V_m$  is the molar volume,  $T$  is the temperature, and



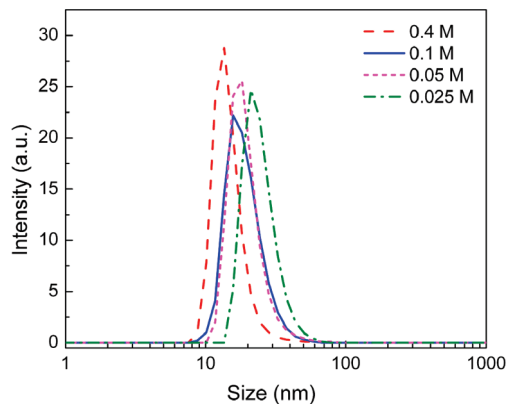


**Figure 3.** Size distribution of CoFe<sub>2</sub>O<sub>4</sub> nanoparticles synthesized at different Co<sup>2+</sup> ion concentrations of 0.4, 0.1, 0.05, and 0.025 M.

$R$  is the gas constant. When  $(2\gamma V_m/rRT) < 1$ , the exponential term in eq 3 becomes linear. Assuming that the growth rate is determined by diffusion of the solute from the smaller particles to the larger particles

$$\bar{r}^3 - \bar{r}_0^3 = \frac{8\gamma DV_m^2 c_\infty}{9RT} t = At \quad (4)$$

Where  $\bar{r}$  is the average particle size at time  $t$ ,  $\bar{r}_0$  is the average particle size at time zero, and  $A$  is a constant. For production of nanoparticles with narrow size distribution by precipitation process, the nucleation process must be relatively fast whereas the growth process must be slow and the nuclei of all species should be present simultaneously, without subsequent nucleation of smaller particles. The concentration gradients and temperature are predominant factors determining growth rate. During growth, material is supplied to the particle surface via long-distance mass transfer. According to eqs 1 and 2, the nucleated particle radius  $r^*$  is inversely proportionally to the logarithm of ion concentration (activity). Therefore, the concentration of both metal and hydroxyl ions can influence the crystallite size and its shape. Since the activity of OH<sup>-</sup> ion is fixed as 1.04 M, the size variation occurs mainly due to the concentration of Co<sup>2+</sup> and Fe<sup>3+</sup> ions. As the concentration of Co<sup>2+</sup> and Fe<sup>3+</sup> ions increases, the solution reaches supersaturation state rapidly leading to the formation of a large number of initial nuclei, with smaller size in a fixed volume. When the concentration of ions is less, the primary nucleated particles will dissolve in the existing solution. If nucleated particle size is less than the critical radius ( $r^*$ ), then particles will grow further with time due to Oswald ripening process.<sup>51,53</sup> Therefore, at low concentration of ions crystallite size is larger.

Figure 3 shows the average hydrodynamic radii and size distribution of CoFe<sub>2</sub>O<sub>4</sub> nanoparticles at different Co<sup>2+</sup> ion concentrations obtained by dynamic light scattering (DLS). The spatial arrangement of the suspended particles (CoFe<sub>2</sub>O<sub>4</sub>) changes with time due to Brownian motion that leads to a change in speckle pattern of the scattered light from the sample. DLS exploits the Brownian motion of the suspended particles to measure the size and distribution of the particles. Time-autocorrelation function (TCF) method is used to measure such scattered intensity fluctuations  $g^2(\delta t) = \langle I(t)I(t + \delta t) \rangle$  where  $\delta t$  is any arbitrary delay time. However, at very small  $\delta t$ ,  $\lim_{\delta t \rightarrow 0} g^2(\delta t) = \langle I(t)^2 \rangle$ . In a dynamic light scattering experiment we can measure this intensity TCF and in the simplest case the decay is a single exponential function like  $g^2(\delta t) = \exp(-t/\tau)$ .

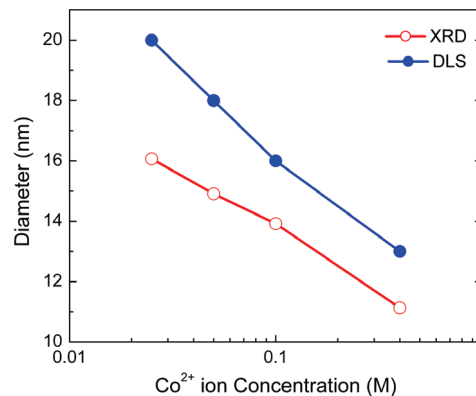


**Figure 4.** Variation of particle size/hydrodynamic size obtained by XRD (open circle) and DLS (solid circle) as a function of Co<sup>2+</sup> ion concentrations.

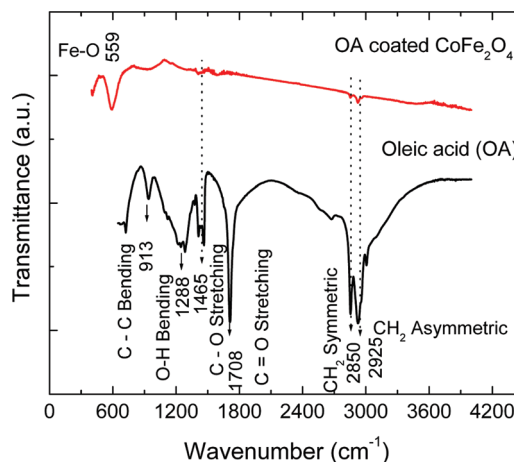


**Figure 5.** FTIR spectra of oleic acid (OA) and OA coated CoFe<sub>2</sub>O<sub>4</sub> nanoparticles synthesized at a Co<sup>2+</sup> concentration of 0.025 M.

The relaxation time  $\tau$ , at which  $g^2(\delta t)$  has decayed to  $1/e$  of its amplitude, is related to the translational diffusion coefficient  $D$  of the solute particles by  $1/\tau = 2Dq^2$ . This refers to the TCF of the electric field  $g^1(\delta t)$ . From the diffusion coefficient the hydrodynamic radius ( $R_H$ ) of the solute particles can be calculated using the Stokes–Einstein equation<sup>54</sup>

$$R_H = \frac{k_B T}{6\pi\eta D} \quad (5)$$

Here  $k_B$  is the Boltzmann constant and  $\eta$  is the viscosity of the solvent. The average size of particles and  $R_H$  obtained by XRD and DLS as a function of metal ion concentration is plotted in Figure 4. The higher value of average size (compared to XRD) obtained in DLS originates from the fact that DLS measures the hydrodynamic radii of the particles, which includes the surfactant and solvent layer at the interface.

**B. FTIR.** The binding of oleic acid on CoFe<sub>2</sub>O<sub>4</sub> surface was examined by Fourier transform infrared spectroscopy (FTIR). Figure 5 shows the FTIR spectrum of pure oleic acid (OA) and OA coated CoFe<sub>2</sub>O<sub>4</sub> nanoparticles. The FTIR spectra of OA shows a series of characteristic peaks at 1708 (C=O stretching of carboxylic headgroup) and 1465 cm<sup>-1</sup> and 1288 cm<sup>-1</sup> is due to the C–O stretching and O–H bending respectively. Further, characteristic vibrations at 2926 and 2853 cm<sup>-1</sup> are attributed to the stretching of asymmetric and symmetric vibrations of

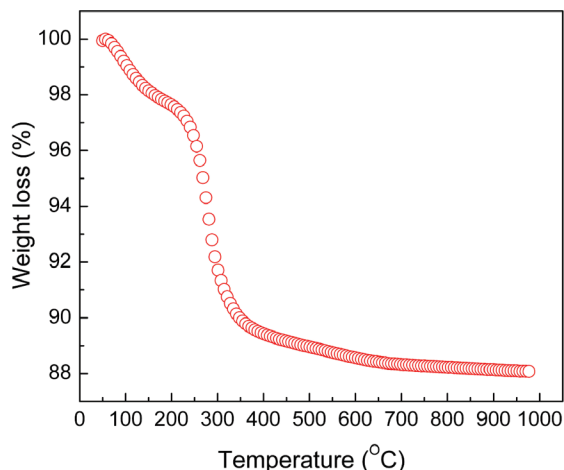


**Figure 6.** Thermogravimetric curve (under air atmosphere) of oleic acid coated  $\text{CoFe}_2\text{O}_4$  nanoparticles synthesized at a  $\text{Co}^{2+}$  ion concentration of 0.025 M.

( $-\text{CH}_2-$ ) group of oleic acid respectively.<sup>55</sup> FTIR spectra of OA coated  $\text{CoFe}_2\text{O}_4$  nanoparticles consists of characteristic peaks at 594, 1413, 1583, 2924, and 3471  $\text{cm}^{-1}$ . The peak at 594  $\text{cm}^{-1}$  corresponds to stretching of Fe–O bond<sup>56</sup> and a broad peak at 3460  $\text{cm}^{-1}$  can be attributed to hydroxide ion stretching that originate from moisture content in the sample. OA coated  $\text{CoFe}_2\text{O}_4$  nanoparticles show two distinct vibrations at 1413 and 1583  $\text{cm}^{-1}$  and are attributed to symmetric and asymmetric vibrations of  $\text{COO}^-$  receptively.<sup>57,58</sup> The disappearance of  $-\text{COOH}$  characteristic peaks suggests that nonexistence of the physically absorbed oleic acid in the samples and the formation of monolayer of oleic acid on the surface of  $\text{CoFe}_2\text{O}_4$  nanoparticles.

**C. Thermogravimetric Analysis (TGA).** Thermogravimetric measurement (Figure 6) shows two-step weight loss in oleic acid coated  $\text{CoFe}_2\text{O}_4$  nanoparticles synthesized at 0.025 M  $\text{Co}^{2+}$  ion concentration. Initial weight loss of 2%, observed in the temperature range of 30–150  $^\circ\text{C}$  corresponds to loss of moisture and volatile components present in the sample. In the temperature range of 160–400  $^\circ\text{C}$ , the second weight loss is nearly 10%, which is due to the oleic acid decomposition. Therefore, the total weight loss in the system is about 12%. This means, only 88% of the sample contributes to the magnetization measurements. The corrected (after removing oleic acid contribution) hysteresis loop and saturation magnetization with crystallite size are plotted in Figures 7 and 8, respectively. For a close-packed monolayer of the surfactant on the surface of spherical nanoparticles of diameter  $d$ , oleic acid molecules occupy a surface area  $a$ , and the surface area per particle is  $\pi d^2$ . The total number of particles is then given by

$$\frac{(100 - W)}{\rho(\pi d^3/6)} \quad (6)$$

where  $W$  is the weight of the surfactant in percentage and  $\rho$  is the density of the particle. The total surfactant molecules in the system are  $WN_0/M$ , where,  $N_0$  is Avogadro number and  $M$  is the molecular weight of the surfactant. Therefore, the surface area  $a$  occupied by oleic acid molecules is the ratio of total surface area on particles to the number of surfactant molecules

$$a = \frac{6(100 - W)M}{N_0 d \rho W} \quad (7)$$

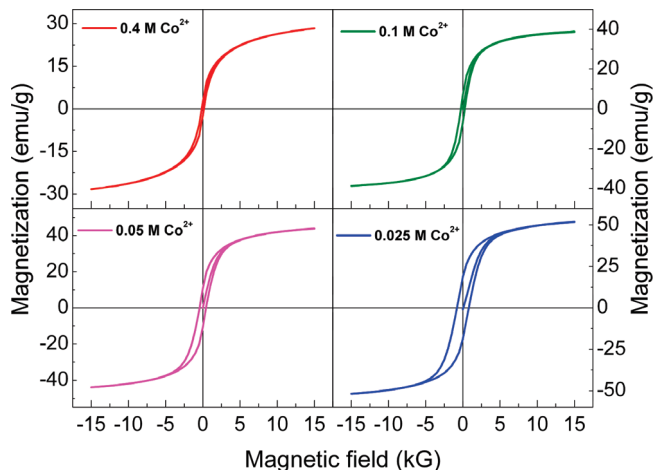


**Figure 7.** Room temperature magnetization curves of  $\text{CoFe}_2\text{O}_4$  synthesized at different  $\text{Co}^{2+}$  ion concentration.

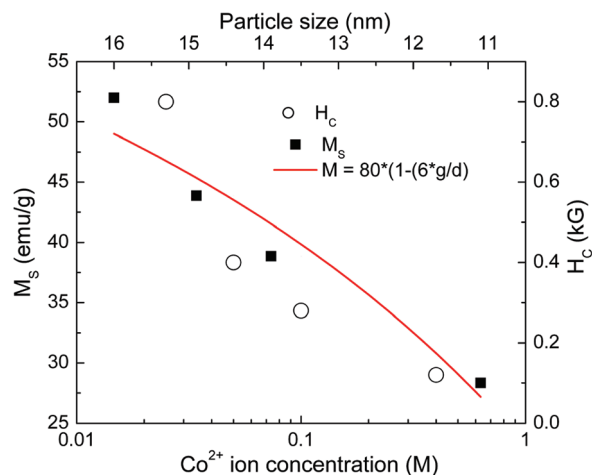


**Figure 8.** Saturation magnetization (solid square, left axis) and coercivity (open circle, right axis) of  $\text{CoFe}_2\text{O}_4$  nanoparticles as a function of  $\text{Co}^{2+}$  metal ions concentration and particle size. The solid line shows the best fit using eq 8 where the  $g$  value obtained from the best fit is 1.3 nm.

The calculated total surface area of oleic acid molecule on  $\text{CoFe}_2\text{O}_4$  surface is 0.28  $\text{nm}^2$  (for  $W = 12\%$ ,  $M = 282$ ,  $d = 14$  nm, and  $\rho = 5.18$   $\text{g cm}^{-3}$ ). The observed value of surface area is in good agreement with the reported value of 0.3  $\text{nm}^2$  for particles of diameter 10 nm having a mono layer coating of oleic acid.<sup>59</sup> Therefore, it can be fairly assumed that the surfactant forms a monolayer on individual nanoparticles.

**D. Magnetic Properties.** Figure 7 shows the room temperature magnetization curves of the  $\text{CoFe}_2\text{O}_4$  nanoparticles prepared with different concentrations of  $\text{Co}^{2+}$  metal ion. Ferromagnetic behavior with minimum coercivity ( $H_c$ ) of 0.12 kG is achieved at 0.4 M of  $\text{Co}^{2+}$  ion. As the  $\text{Co}^{2+}$  ion concentration is reduced, the particle size increases due to Oswald ripening, and the magnetization curves show ferromagnetic behavior with finite coercivity values. The single-domain and superparamagnetic diameters for  $\text{CoFe}_2\text{O}_4$  nanoparticles corresponds to 40 and 10 nm, respectively. The slight coercivity of 0.12 kG (0.4 M of  $\text{Co}^{2+}$  ion) reaffirms that the particle diameter is more than the superparamagnetic limit. Figure 8 shows the monotonic increment in saturation magnetization ( $M_s$ ) and  $H_c$  with crystallite size (excluding oleic acid contribution). The  $M_s$  and  $H_c$  increases from 28 to 52 emu/g and from 0.12 to 0.8 kG, respectively, as the crystallite size increases from 11 to 16 nm. The measured  $M_s$  value of 52 emu/g for 16 nm sized

**TABLE 1: Reported Literature Values of Saturation Magnetization ( $M_s$ ), Coercivity ( $H_c$ ), Remanence ( $M_r$ ), Blocking Temperature ( $T_B$ ), and Anisotropy Constant ( $K$ ) of CoFe<sub>2</sub>O<sub>4</sub> Nanoparticles**

average particle size (nm)		$M_s$ (emu/g)	$H_c$ (kOe)	$M_r$ (emu/g)	$T_B$ (K)	$K$	ref
XRD	TEM						
2					100	$4 \times 10^7$ (erg/cm <sup>3</sup> )	24
3					160	$1 \times 10^7$ (erg/cm <sup>3</sup> )	24
5.5	5.9	65 (300 K)			300	$1.6 \times 10^7$ (erg/cm <sup>3</sup> )	43
		85.1 (5K)	9.3 (5K)				
4.3		14			250		61
12	14	64.7 (300K)	0.05		390		23
		81 (5K)	9.4 (5K)				
12	10–20	68	1				22
	240	70	5.1	~33			
20		20		1.31			62
22		57	0.086	4.29			
12	10–50	38	1.59				36
24	10–50	57	4.6				
20	~20	7.1	9.47			$7.33 \times 10^5$ J/m <sup>3</sup>	39
56		74.2	0.93				
11		28	0.12	2.4			present study
16	14.8	52	0.80	18.7			

particle (corresponding to a Co<sup>2+</sup> concentration of 0.025 M) was comparable to the value reported for cobalt ferrite nanoparticles of same size.<sup>36</sup> The measured value of  $M_s$  is considerably less than that of the multidomain bulk CoFe<sub>2</sub>O<sub>4</sub> materials saturation magnetization of 72 emu/g. Shafi et al.<sup>60</sup> prepared CoFe<sub>2</sub>O<sub>4</sub> nanoparticles of average particle diameter less than 10 nm, by a sonochemical approach, show magnetization values between 22 and 45 emu/g under different annealing conditions. Recently Limaye et al reported high coercivity of oleic acid coated CoFe<sub>2</sub>O<sub>4</sub> nanoparticles (9.47 kOe) which is attributed to magnetic anisotropy, strain, and disorder of the surface spins of CoFe<sub>2</sub>O<sub>4</sub> nanoparticles.<sup>39</sup> In case of thin films of 50 nm, a coercivity value of 9.3 kOe is achieved by Wang et al.<sup>40</sup> They suggest that lattice strain during annealing at 900 °C for 15 min induces large magnetic anisotropy and high coercivity in CoFe<sub>2</sub>O<sub>4</sub> thin films. Jung et al.<sup>3</sup> have shown that the high coercivity of 14 kOe in CoFe<sub>2</sub>O<sub>4</sub> nanowire is due to the formation of clustering of nanoparticles after annealing at 600 °C for 2 h. The high coercivity of 5.1 kOe in CoFe<sub>2</sub>O<sub>4</sub> nanoparticles is attributed to the large strain and defective microstructure during milling for 1.5 h.<sup>22</sup> A modified coprecipitation technique is developed to controls the growth of cobalt ferrite nanocrystals with coercivity varying from 460 to 4626 Oe.<sup>36</sup> In the case of noninteracting CoFe<sub>2</sub>O<sub>4</sub>–SiO<sub>2</sub> nanocomposites, high coercivity of the order of 14 kOe is observed at low temperature.<sup>18,41</sup> These studies clearly illustrate that magnetocrystalline anisotropy, lattice strain, surface spin canting, and synthesis methods play an important role in regulating the coercivity of CoFe<sub>2</sub>O<sub>4</sub> nanoparticles. The reported values of magnetic properties (saturation magnetization, coercivity, remanence, etc.) of cobalt ferrites synthesized by various techniques have a broad range values and are listed in Table 1.

The value of squareness ration ( $M_r/M_s$ ) provides a rough means by which exchange interaction and magnetocrystalline anisotropy can be studied. The squareness ratios for CoFe<sub>2</sub>O<sub>4</sub> nanoparticles synthesized with Co<sup>2+</sup> ion concentrations of 0.4, 0.1, 0.05, and 0.025 M are 0.08, 0.178, 0.245, and 0.36, respectively. Grigorova et al.<sup>61</sup> found similar results for 6.6 nm CoFe<sub>2</sub>O<sub>4</sub> nanoparticles annealed at 370 °C. The same trend was observed by Jeppson and co-workers.<sup>62</sup> This indicates that magnetocrystalline anisotropy is not the only parameter that is responsible for low coercivity and remanence values. Momen et al.<sup>24</sup> and Tung et al.<sup>63</sup> reported that the  $M_r/M_s$  is 0.5 for ultra fine CoFe<sub>2</sub>O<sub>4</sub> nanoparticles which indicates the cubic magne-

tocrystalline anisotropy is predominant. The decrease in the saturation magnetization with decreasing crystalline size is usually explained in terms of spin disorders or dead layer at or near the surface of the particles. The pronounced surface spin disorder effect of ultra fine nanoparticles (less than 5 nm), produced using novel preparation procedures, on physical properties have been reported.<sup>24</sup> Tang et al.<sup>64</sup> have shown that the grain boundaries or dead layer shell thickness ( $g$ ) can lead to a reduction in  $M_s$  with size. The correlation between the crystallite size and  $M_s$  is given as

$$M_s = M_{s(\text{bulk})} \left( 1 - \frac{6g}{d} \right) \quad (8)$$

The obtained value of dead layer thickness from the best fit is about 1.3 nm, in good agreement with our earlier HRTEM studies (Figure 8). Reported values of  $g$  range from 0.5 to 1.5 nm.<sup>10,65,66</sup> Apart from dead layer due to the size decrement,<sup>67</sup> the impurity phases such as ferrihydrides, FeOOH, Co(OH)<sub>2</sub>, etc. can also cause a reduction in the saturation magnetization values.

Even though XRD shows no other impurity phases, possibilities for the presence of other impurity phases like ferrihydrite and Co(OH)<sub>2</sub> (JCPDS card no. 74-1057) exist. The peaks due to the above phases can be overlapped with that of CoFe<sub>2</sub>O<sub>4</sub>. It has been reported that rapid hydrolysis of Fe(III) solution can lead to the formation of ferrihydrite.<sup>45</sup> Modest heating of the Fe(III) solutions at 80 °C typically produces 6-line ferrihydrite, whereas the 2-line ferrihydrite is produced at ambient temperatures, during the addition of alkali. The X-ray diffraction pattern of 2-line ferrihydrite shows two peaks at 2.59 and 1.48 Å  $d$  spacing, corresponding to 35.43 and 65.58°. Peaks of 2 or 6-line ferrihydrite overlap with the standard peaks of CoFe<sub>2</sub>O<sub>4</sub> phase. Our earlier study shows that during precipitation, ferrihydrite is formed when alkali (6 N NaOH) is added rapidly at 90 °C.<sup>30</sup> Impurity phases like ferrihydrite cannot be distinguished from CoFe<sub>2</sub>O<sub>4</sub> phase from the XRD pattern. Therefore, micro Raman spectrum is employed to check the presence of impurities in the CoFe<sub>2</sub>O<sub>4</sub> nanoparticles synthesized at different metal ion concentrations.

**E. Micro Raman Spectroscopy.** In spinel ferrite, distribution of divalent and trivalent cations can change due to migration of metal ions from tetrahedral (A) to octahedral (B) sites and



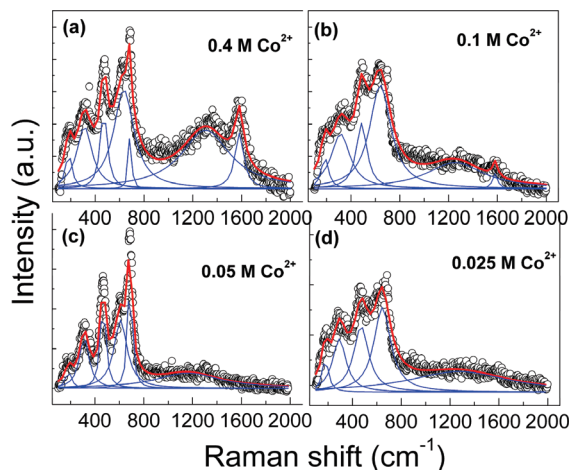


**Figure 9.** Room temperature micro Raman spectra of  $\text{CoFe}_2\text{O}_4$  synthesized at  $\text{Co}^{2+}$  metal ion concentrations of (a) 0.4, (b) 0.1, (c) 0.05, and (d) 0.025 M.

vice versa. Mossbauer spectroscopy is widely used to study ion migration in spinel ferrites.<sup>69</sup> The poor resolution due to overlapping of the peaks corresponding to A and B sites sometimes makes the analysis difficult. Raman spectroscopy is a highly sensitive tool for many lattice effects, such as structure transition, lattice distortion, charge–lattice and spin–lattice couplings, local cation distribution, and magnetic ordering.<sup>70</sup> Raman scattering is widely recognized as a powerful tool for probing magnetic oxides.  $\text{CoFe}_2\text{O}_4$  has an inverse cubic spinel structure and belongs to the space group of  $O_h^7$  ( $Fd3m$ ). The full unit cell contains 56 atoms but the smallest Bravais cell contains only 14 atoms. Therefore, 42 vibrational modes are possible. Group theory predicts five Raman active modes, i.e.,  $A_{1g} + E_g + 3T_{2g}$ .<sup>71</sup> Raman spectra of  $\text{CoFe}_2\text{O}_4$  nanoparticles prepared at different  $\text{Co}^{2+}$  ion concentrations are shown in Figure 9. Room temperature Raman spectra at different  $\text{Co}^{2+}$  ion concentrations of 0.4, 0.1, 0.05, and 0.025 M consists of broad bands at  $\sim 186$ ,  $\sim 312$ ,  $\sim 477$ , 1330, and  $1580\text{ cm}^{-1}$ , and strong bands at  $\sim 634$  and  $\sim 687\text{ cm}^{-1}$  in the frequency range of  $2000\text{--}100\text{ cm}^{-1}$ . The best fitting on the spectra using Lorentzian shaped lines gives five peak positions of Raman spectra. All the observed peaks are similar to the bulk maghemite phase and the peaks are shifted to the lower wavenumber compared to maghemite owing to the higher mass of Co compared to Fe. By comparing the observed peak positions with the earlier reports on  $\text{CoFe}_2\text{O}_4$ ,<sup>30,37,39</sup> the peaks at  $\sim 190$  and  $\sim 306\text{ cm}^{-1}$  illustrates the  $T_{1g}$  and  $E_g$  modes respectively. Peak at  $\sim 477$  is assigned to  $T_{2g}$  mode corresponding to the local symmetry vibrations of metal ions in the octahedral site. We observed two strong bands at  $\sim 630$  and  $\sim 690\text{ cm}^{-1}$  against the reported single band value of  $\sim 651\text{ cm}^{-1}$  for  $A_{1g}$  symmetry vibrations of metal ion in tetrahedral site and  $710\text{ cm}^{-1}$  band of 2-line ferrihydrite. Apart from five optical phonon modes, we observe two additional peaks at 1320 and  $1580\text{ cm}^{-1}$  (for 0.4 and 0.1 M of  $\text{Co}^{2+}$ ) that corresponds to ferrihydrite phase. Ferrihydrite peak intensity decreases considerably as the metal ion concentration is decreased from 0.4 to 0.1 M and vanishes at very low metal ion activities. Earlier reports show that the bands at 1320 and  $1580\text{ cm}^{-1}$  is due the magnetite-like modification of ferrihydrite.<sup>72</sup> Formation of ferrihydrite decreases the symmetry in B-site that results in the doublet at  $650\text{--}700\text{ cm}^{-1}$ . These experimental results suggest that the metal ion activity plays an important role in the size, purity and the magnetic properties of the  $\text{CoFe}_2\text{O}_4$  nanoparticles.

#### IV. Conclusions

We have studied the effect of  $\text{Co}^{2+}$  ion concentration on crystal size, purity and magnetic properties of  $\text{CoFe}_2\text{O}_4$  nanoparticles. The average crystallite size, coercivity ( $H_c$ ) and saturation magnetization ( $M_s$ ) increases from 11 to 16 nm, 0.12 to 0.8 kOe and 28 to 52 emu/g respectively as  $\text{Co}^{2+}$  metal ion concentration decreases from 0.4 to 0.025 M. Formation of paramagnetic ferrihydrite at high metal ion concentration is confirmed by micro Raman spectroscopy. Further our Raman spectroscopy results suggest that the presence ferrihydrite, which is untraceable by XRD, leads to a reduction in saturation magnetization. Our findings suggest that less than 0.1 M  $\text{Co}^{2+}$  ion concentration is ideal to obtain  $\text{CoFe}_2\text{O}_4$  nanoparticles without impurity phases.

**Acknowledgment.** Authors would like to thank Dr. R. Divakar, Dr. E. Mohandas and Dr. M. Vijayalakshmi for HRTEM and Dr. K. S. Viswanathan and Mr. N. Ramanathan for AAS and FTIR measurements. We thank Dr. P. R. Vasudev Rao and Dr. T. Jayakumar for encouragement and support.

#### References and Notes

- (1) Min, Y.; Akbulut, M.; Kristiansen, K.; Golan, Y.; Israelachvili, J. *Nat. Mater.* **2007**, *7*, 527.
- (2) Dorman, J. L.; Fiorani, D. *Magnetic Properties of fine particles*; North Holland: Amsterdam, 1992.
- (3) Jung, J.-S.; Lim, J.-H.; Choi, K.-H.; Oh, S.-L.; Kim, Y.-R.; Lee, S.-H.; Smith, D. A.; Stokes, K. L.; Malkinski, L.; O'Connor, C. J. *J. Appl. Phys.* **2005**, *97*, 10F306.
- (4) Qi, H.; Chen, Q.; Wang, M.; Wen, M.; Xiong, J. *J. Phys. Chem. C* **2009**, *113*, 17301.
- (5) Oliveira, F. C. C.; Rossi, L. M.; Jardim, R. F.; Rubim, J. C. *J. Phys. Chem. C* **2009**, *113*.
- (6) Che, R. C.; Zhi, C. Y.; Liang, C. Y.; Zhou, X. G. *Appl. Phys. Lett.* **2006**, *88*, 033105.
- (7) Kim, C. H.; Myung, Y.; Cho, Y. J.; Kim, H. S.; Park, S.-H.; Park, J.; Kim, J.-Y.; Kim, B. *J. Phys. Chem. C* **2009**, *113*, 7085.
- (8) Peng, C.-H.; Wang, H.-W.; Shih-Wei Kanb, M.-Z. S.; Wei, Y.-M.; Chen, S.-Y. *J. Magn. Magn. Mater.* **2004**, *284*, 113.
- (9) Philip, J.; Gnanaprakash, G.; Jayakumar, T.; Kalyanasundaram, P.; Raj, B. *Macromolecules* **2003**, *36*, 9230.
- (10) Philip, J.; Shima, P. D.; Raj, B. *Appl. Phys. Lett.* **2007**, *92*, 043108.
- (11) Pankhurst, Q. A.; Connolly, J.; Jones, S. K.; Dobson, J. *J. Phys. D: Appl. Phys.* **2003**, *36*, R167.
- (12) Morais, P. C. *J. Alloys Compd.* **2009**, *483*, 544.
- (13) Kang, K.; Choi, J.; Nam, J. H.; Lee, S. C.; Kim, K. J.; Lee, S.-W.; Chang, J. H. *J. Phys. Chem. B* **2009**, *113*.
- (14) Mu, Q.; Li, Z.; Li, X.; Mishra, S. R.; Zhang, B.; Si, Z.; Yang, L.; Jiang, W.; Yan, B. *J. Phys. Chem. C* **2009**, *113*, 5390.
- (15) Joshi, H. M.; Lin, Y. P.; Aslam, M.; Prasad, P. V.; Schultz-Sikma, E. A.; Edelman, R.; Meade, T.; Dravid, V. P. *J. Phys. Chem. C* **2009**, *113*, 17761.
- (16) Kim, D.-H.; Nikles, D. E.; Johnson, D. T.; Brazel, C. S. *J. Magn. Magn. Mater.* **2008**, *320*, 2390.
- (17) Song, Q.; Zhang, Z. J. *J. Am. Chem. Soc.* **2004**, *126*, 6164.
- (18) Peddis, D.; Mansilla, M. V.; Mørup, S.; Cannas, C.; Musinu, A.; Piccaluga, G.; D'Orazio, F.; Lucari, F.; Fiorani, D. *J. Phys. Chem. B* **2008**, *112*, 8507.
- (19) Bao, N.; Shen, L.; An, W.; Padhan, P.; Turner, C. H.; Gupta, A. *Chem. Mater.* **2009**, *21*, 3458.
- (20) Sun, S.; Zeng, H.; Robinson, D. B.; Raoux, S.; Rice, P. M.; Wang, S. X.; Li, G. *J. Am. Chem. Soc.* **2004**, *126*, 273.
- (21) Jia, X.; Chen, D.; Jiao, X.; He, T.; Wang, H.; Jiang, W. *J. Phys. Chem. C* **2008**, *112*, 911.
- (22) Liu, B. H.; Ding, J.; Dong, Z. L.; Boothroyd, C. B.; Yin, J. H.; Yi, J. B. *Phys. Rev. B* **2006**, *74*, 184427.
- (23) Manova, E.; Kunev, B.; Paneva, D.; Mitov, I.; Petrov, L.; Estournes, C.; D'Orleans, C.; Rehspringer, J.-L.; Kurmoo, M. *Chem. Mater.* **2004**, *16*, 5689.
- (24) Moumen, N.; Bonville, P.; Pileni, M. P. *J. Phys. Chem.* **1996**, *100*, 14410.
- (25) Cannas, C.; Ardu, A.; Musinu, A.; Peddis, D.; Piccaluga, G. *Chem. Mater.* **2008**, *20*, 6364.
- (26) Pramanik, N. C.; Fujii, T.; Nakanishi, M.; Takada, J. *J. Mater. Chem.* **2004**, *14*, 3328.



- (27) Lee, D. K.; Kim, Y. H.; Kang, Y. S.; Stroeve, P. *J. Phys. Chem. B* **2005**, *109*, 14939.
- (28) Coker, V. S.; Telling, N. D.; Laan, G. v. d.; Patrick, R. A. D.; Pearce, C. I.; Arenholz, E.; Tuna, F.; Winpenny, R. E. P.; Lloyd, J. R. *ACS Nano* **2009**, *3*, 1922.
- (29) Zhao, S.-Y.; Qiao, R.; Zhang, X. L.; Kang, Y. S. *J. Phys. Chem. C* **2007**, *111*, 7875.
- (30) Ayyappan, S.; Philip, J.; Raj, B. *J. Phys. Chem. C* **2009**, *113*, 590.
- (31) Yang, H.; Ogawa, T.; Hasegawa, D.; Takahashi, M. *J. Appl. Phys.* **2008**, *103*, 07D526.
- (32) Wang, Z.; Liu, X.; Lv, M.; Chai, P.; Liu, Y.; Meng, J. *J. Phys. Chem. B* **2008**, *112*, 11292.
- (33) Cushing, B. L.; Kolesnichenko, V. L.; O'Connor, C. J. *Chem. Rev.* **2004**, *104*, 3893.
- (34) Morais, P. C.; Garg, V. K.; Oliveira, A. C.; Silva, L. P.; Azevedo, R. B.; Silva, A. M. L.; Lima, E. C. D. *J. Magn. Magn. Mater.* **2001**, *225*, 37.
- (35) Lin, C.-R.; Wang, C.-C.; Chen, I.-H. *J. Magn. Magn. Mater.* **2006**, *304*, e34.
- (36) Cedeno-Mattei, Y.; Perales-Perez, O.; Tomar, M. S.; Roman, F.; Voyles, P. M.; Stratton, W. G. *J. Appl. Phys.* **2008**, *103*, 07E512.
- (37) Soler, M. A. G.; Lima, E. C. D.; Silva, S. W. d.; Melo, T. F. O.; Pimenta, A. C. M.; Sinnecker, J. P.; Azevedo, R. B.; Garg, V. K.; Oliveira, A. C.; Novak, M. A.; Morais, P. C. *Langmuir* **2007**, *23*, 9611.
- (38) Sear, R. P. *J. Phys. Chem. B* **2006**, *110*, 4985.
- (39) Limaye, M. V.; Singh, S. B.; Date, S. K.; Kothari, D.; Reddy, V. R.; Gupta, A.; Sathe, V.; Choudhary, R. J.; Kulkarni, S. K. *J. Phys. Chem. B* **2009**, *113*, 9070.
- (40) Wang, Y. C.; Ding, J.; Yi, J. B.; Liu, B. H.; Yu, T.; Shen, Z. X. *Appl. Phys. Lett.* **2004**, *84*, 2596.
- (41) Casu, A.; Casula, M. F.; Corrias, A.; Falqui, A.; Loche, D.; Marras, S. *J. Phys. Chem. C* **2007**, *111*, 916.
- (42) Ngo, A. T.; Bonville, P.; Pilenia, M. P. *J. Appl. Phys.* **2001**, *89*, 3370.
- (43) Ammar, S.; Helfen, A.; Jouini, N.; Fievet, F.; Rosenman, I.; Villain, F.; Molinie, P.; Danot, M. *J. Mater. Chem.* **2001**, *11*, 186.
- (44) Hu, G.; Choi, J. H.; Eom, C. B.; Harris, V. G.; Suzuki, Y. *Phys. Rev. B* **2000**, *62*, R779.
- (45) Jambor, J. L.; Dutrizac, J. E. *Chem. Rev.* **1998**, *98*, 2549.
- (46) Gu, Z.; Xiang, X.; Fan, G.; Li, F. *J. Phys. Chem. C* **2008**, *112*, 18459.
- (47) Chakraverty, S.; Mitra, S.; Mandal, K.; Nambissan, P. M. G.; Chattopadhyay, S. *Phys. Rev. B* **2005**, *71*, 024115.
- (48) Nambissan, P. M. G.; Upadhyay, C.; Verma, H. C. *J. Appl. Phys.* **2003**, *93*, 6320.
- (49) Stoneham, A. M. *J. Phys. C: Solid State Phys.* **1977**, *10*, 1175.
- (50) Woltersdorf, J.; Nepijko, A. S.; Pippel, E. *Surf. Sci.* **1981**, *106*, 64.
- (51) Lifshitz, I. M.; Sloyozov, V. V. *J. Phys. Chem. Solids* **1961**, *19*, 35.
- (52) Oskam, G.; Nellore, A.; Penn, R. L.; Searson, P. C. *J. Phys. Chem. B* **2003**, *107*, 1734.
- (53) Yin, M.; O'Brien, S. *J. Am. Chem. Soc.* **2003**, *125*, 10180.
- (54) Kohoutek, T.; Wagner, T.; Frumar, M.; Chrissanthopoulos, A.; Kostadinova, O.; Yannopoulos, S. N. *J. Appl. Phys.* **2008**, *103*, 063511.
- (55) Gnanaprakash, G.; Philip, J.; Jayakumar, T.; Raj, B. *J. Phys. Chem. B* **2007**, *111*, 7978.
- (56) Waldron, R. D. *Phys. Rev.* **1955**, *99*, 1727.
- (57) Willis, A. L.; Turro, N. J.; O'Brien, S. *Chem. Mater.* **2005**, *17*, 5970.
- (58) Kirwan, L. J.; Fawell, P. D.; Bronswijk, W. v. *Langmuir* **2004**, *20*, 4093.
- (59) Ewijk, G. A. V.; Vroege, G. J.; Philipse, A. P. *J. Magn. Magn. Mater.* **1999**, *201*, 31.
- (60) Shafi, K. V. P. M.; Gedanken, A.; Prozorov, R.; Balogh, J. *Chem. Mater.* **1998**, *10*, 3445.
- (61) Grigorova, M.; Blythe, H. J.; Blaskov, V.; Rusanov, V.; Petkov, V.; Masheva, V.; Nihtianova, D.; Martinez, L. M.; Munoz, J. S.; Mikhov, M. *J. Magn. Magn. Mater.* **1998**, *183*, 163.
- (62) Jeppson, P.; Sailer, R.; Jarabek, E.; Sandstrom, J.; Anderson, B.; Bremer, M.; Grier, D. G.; Schulz, D. L.; Caruso, A. N.; Payne, S. A.; Eames, P.; Tondra, M.; He, H.; Chrisey, D. B. *J. Appl. Phys.* **2006**, *100*, 114324.
- (63) Tung, L. D.; Kolesnichenko, V.; Caruntu, D.; Chou, N. H.; O'Connor, C. J.; Spinu, L. *J. Appl. Phys.* **2003**, *93*, 7486.
- (64) Tang, Z. X.; Sorensen, C. M.; Klabunde, K. J. *Phys. Rev. Lett.* **1991**, *67*, 3602.
- (65) Dutta, P.; Pal, S.; Seehra, M. S.; Shah, N.; Huffman, G. P. *J. Appl. Phys.* **2009**, *105*, 07B501.
- (66) Kodama, R. H.; Berkowitz, A. E.; McNiff, E. J., Jr.; Foner, S. *J. Appl. Phys.* **1997**, *81*, 5552.
- (67) Kim, T.; Shima, M. *J. Appl. Phys.* **2007**, *101*, 09M516.
- (68) Drits, V. A.; Sakharov, B. A.; Salyn, A. L.; Manceau, A. *Clay. Miner.* **1993**, *28*, 185.
- (69) Hamdeh, H. H.; Hikal, W. M.; Taher, S. M.; Ho, J. C.; Thuy, N. P.; Quy, O. K.; Hanh, N. *J. Appl. Phys.* **2005**, *97*, 064310.
- (70) Yu, T.; Shen, Z. X.; Shi, Y.; Ding, J. *J. Phys.: Condens. Matter* **2002**, *14*, L613.
- (71) Gasparov, L. V.; Tanner, D. B.; Romero, D. B.; Berger, H.; Margaritondo, G.; Forro, L. *Phys. Rev. B* **2000**, *62*, 7939.
- (72) Mazzetti, L.; Thistlethwaite, P. J. *J. Raman Spectrosc.* **2002**, *33*, 104.